A neural network-based scale-adaptive cloud-fraction scheme for GCMs

Guoxing Chen^{1,2,3*}, Wei-Chyung Wang⁴, Shixi Yang¹, Yixin Wang¹, Feng Zhang^{1,2,3}, and Kun Wu⁵

Key Points (<140 characters):

- A neural network-based scheme for parameterizing sub-grid cloud fraction in climate models is developed using the CloudSat data.
- The scheme considers the effects of both horizontal and vertical grid sizes on cloud-fraction parameterization.
- The scheme better predicts total cloud-fraction spatial distribution and cloud vertical structure than the Xu-Randall scheme.

¹Department of Atmospheric and Oceanic Sciences & Institute of Atmospheric Sciences, Fudan University, Shanghai, China

²Shanghai Qi Zhi Institute, Shanghai, China

³Shanghai Frontier Science Center of Atmosphere-Ocean Interaction, Fudan University, Shanghai, China

⁴Atmospheric Sciences Research Center, University at Albany, State University of New York, New York, USA

⁵Key Laboratory of Meteorological Disaster, Ministry of Education/Collaborative Innovation Center on Forecast and Evaluation of Meteorological Disasters, Nanjing University of Information Science and Technology, Nanjing, China

^{*}Corresponding author: Guoxing Chen (chenguoxing@fudan.edu.cn)

Abstract

Cloud fraction significantly affects the short- and long-wave radiation. Its realistic representation in general circulation models (GCMs) still poses great challenges in modeling the atmosphere. Here, we present a neural network-based diagnostic scheme that uses the grid-mean temperature, pressure, liquid and ice water mixing ratios, and relative humidity to simulate the sub-grid cloud fraction. The scheme, trained using CloudSat data with explicit consideration of grid sizes, realistically simulates the observed cloud fraction with a correlation coefficient (r) > 0.9 for liquid-, mixed-, and ice-phase clouds. The scheme also captures the observed non-monotonic relationship between cloud fraction and relative humidity and is computationally efficient, and robust for GCMs with a variety of horizontal and vertical resolutions.

For illustrative purposes, we conducted comparative analyses of the 2006-2019 climatological-mean cloud fractions among CloudSat, and simulations from the new scheme and the Xu-Randall scheme (optimized the same way as the new scheme). The network-based scheme improves not only the spatial distribution of the total cloud fraction but also the cloud vertical structure (r > 0.99). For example, the biases of too-many high-level clouds over the tropics and too-many low-level clouds over regions around 60° S and 60° N in the Xu-Randall scheme are significantly reduced. These improvements are also found to be insensitive to the spatio-temporal variability of large-scale meteorology conditions, implying that the scheme can be used in different climate regimes.

Plain Language Summary

The clouds reflecting shortwave radiation and absorbing/emitting longwave radiation are all sensitive to the cloud fraction. However, the simulation of cloud fraction in GCMs has been difficult, because most clouds are smaller than the typical scales of GCM grids and cannot be resolved by the grid-scale physics, while the physical understanding of sub-grid processes is still inadequate. Thus, this study uses a data-driven approach, i.e., the neural network, to parameterize the sub-grid cloud fraction in climate models. The database for training and evaluating this new scheme is obtained by upscaling the CloudSat (quasi-) observational data and emulating the GCM 'grid-mean' properties required for cloud-fraction parameterization, minimizing the data-oriented biases. Moreover, the effects of the GCM horizontal and vertical grid sizes are both considered in the network, increasing the scheme adaptivity for use in GCMs with different resolutions. Results show that the new scheme correctly predicts observed features of cloud-fraction variation with cloud condensate content and relative humidity for clouds of different phases and better predicts total cloud-fraction spatial distribution and cloud vertical structure than the conventional Xu-Randall scheme. This suggests that the new scheme has great potential to reduce the biases of cloud radiative effects existing in current GCMs.

1 Introduction

Clouds play important roles in the Earth climate system. They dominate the energy budget by reflecting shortwave radiation and trapping longwave radiation (Wild et al., 2019),

participate in the hydrological cycle via precipitation, and alter mass and energy vertical profiles by cloud venting (Yin et al., 2005; Chen et al., 2012a) and latent-heat release. On the other hand, clouds are strongly coupled with aerosols and meteorology (Stevens and Feingold, 2009), involving complex feedback that spans several temporal and spatial scales (e.g., Lau et al., 2006; Xue et al., 2008; Chen et al., 2012b; Chen et al., 2018a, 2018b; Song et al., 2019). However, clouds are sub-grid scale in nature for current climate models, and cloud macro- and micro-physical properties in models have to be parameterized using the grid-mean atmospheric properties, making clouds the main source of most uncertainties in studies on climate change and climate modeling (e.g., Caldwell et al., 2016; Stevens et al., 2016).

Specifically, cloud fraction parameterization poses a major challenge in climate modeling. Findings in the recent Coupled Model Intercomparison Project phase 6 (CMIP6) revealed that current general circulation models (GCMs) have biases in both the daily-mean cloud fraction and the cloud diurnal variation. For example, for the former, the simulated cloud fraction is too small over the tropics, extratropics, and midlatitude regions (Vignesh et al., 2020; Li et al., 2021); and for the latter, the cloud fraction over land is too small during the daytime and too large during the nighttime (Chen & Wang, 2016b; Chen et al., 2022). As the shortwave cloud radiative effect (SWCRE) occurs only during the daytime while the longwave cloud radiative effect (LWCRE) persists throughout the daytime and nighttime, the biases in cloud fraction can affect not only the energy balance but also the energy diurnal variation, which may have implications on atmospheric variations of longer time scales (e.g., Slingo et al., 2003; Ruppert, 2016).

Current parameterization schemes of cloud fraction can be divided into diagnostic and prognostic approaches. In the diagnostic approach, the sub-grid cloud fraction is a function of the instantaneous grid-mean relative humidity and/or cloud water content (e.g., Sundqvist et al., 1989; Xu & Randall, 1996; Shiu et al., 2021). These schemes are easy to implement and computationally efficient, but too empirical. On the other hand, the prognostic approach, which explicitly simulates the temporal variate of cloud fraction using source and sink terms associated with advection, cumulus convection, stratiform condensation, evaporation, and precipitation (Tiedtke, 1993; Wilson et al., 2008; Park et al., 2016), seems more physical. However, all source/sink terms are empirically related to the grid-mean properties, which are difficult to verify with observations. In addition, climate models usually employ different horizontal and vertical resolutions, which may affect the sub-grid statistical characteristics and thus the cloud-fraction parameterization.

In recent years, deep-learning methods have been demonstrated to be an effective alternative approach in atmospheric modeling (Chantry et al., 2021; Schultz et al., 2021). They can help reveal associations among atmospheric parameters by learning directly from data, regardless of inadequate or even none prior domain knowledge. For example, the feedforward neural network (also called multiple-layer perceptron, hereafter denoted as neural network for short) is good at emulating complex functions and can be used to replace certain modules for either accounting for poorly-understood processes or saving computational cost. It has been used to parameterize processes such as cloud cover (Grundner et al., 2022), radiation (Krasnopolsky & Fox-Rabinovitz, 2006), convection (Rasp et al., 2018; Han et al., 2020; T. Zhang et al., 2021), and boundary-layer turbulence (Wang et al., 2019). All yield promising outcomes. For the same reasons, the networks with complex architectures exhibit superiorities in building tools for specific predictions such as El Niño (Nooteboom et al., 2018; Ham et al., 2019), precipitation

(Shi et al., 2015; Ravuri et al., 2021; Chen & Wang, 2022) and clouds (Zhang et al., 2021), and for data processing (Rasp & Lerch, 2018; Leinonen et al., 2021; Kim et al., 2021; Y. Zhang et al., 2021; Pan et al., 2019, 2021, 2022).

In this study, we introduce a neural network-based diagnostic scheme for simulating cloud fraction in climate models. This scheme has advantages in at least three aspects. First, using the neural network avoids the non-physical assumption of formula forms in the parameterization; second, the data for developing the scheme were obtained from CloudSat observations of cloud profiles and the associated large-scale meteorology conditions, minimizing the data-oriented scheme biases; and third, the scale adaptivity (both horizontally and vertically) is considered while developing the scheme so that the scheme has higher robustness across models with different resolutions and in models with varying resolutions (e.g., the Model for Prediction Across Scales-Atmosphere, Skamarock et al., 2012; the Global-to-Regional Integrated forecast SysTem atmosphere model, Zhou et al., 2020).

The rest of this manuscript is arranged as follows: Section 2 describes the data preparation; Sections 3 gives the description of the new scheme and the conventional Xu-Randall scheme (Xu & Randall, 1996), the latter of which is used as a baseline for evaluating the new scheme; Section 4 tests the new scheme in aspects of accuracy and scale adaptivity within the context of a machine-learning study; Section 5 evaluates the new scheme with multiple-year CloudSat data using an offline application; and last the summary and discussion are given in Section 6.

2 Data preparation

2.1 CloudSat

We use the CloudSat data for training, validation, and testing of the network-based cloud-fraction scheme. CloudSat is a polar-orbiting satellite launched by NASA in April 2006. It observes cloud vertical structure along its track using a 95 GHz radar onboard (Stephens et al., 2002). Its data have been widely used previously in studies on cloud climatology (e.g., Weisz et al., 2007; Kato et al., 2010; Chen et al., 2016; Tang et al., 2020), model development (e.g., Di Giuseppe & Tompkins, 2015; Li et al., 2018), and model evaluations (e.g., Bodas-Salcedo et al., 2008; Greenwald et al., 2012; Kodama et al., 2012; Wang & Zhang, 2018; Vignesh et al., 2020).

This study uses 6 variables from 3 CloudSat products: cloud liquid and ice water contents from 2B-CWC-RO (Austin & Wood, 2018); CPR (cloud profiling radar) cloud mask from 2B-GEOPROF (Marchand et al., 2008); atmospheric pressure, temperature, and specific humidity from ECMWF-AUX (Partain, 2022). The data all have a horizontal resolution of 1.1 km and a vertical resolution of 240 m.

Figure 1 presents the availability of CloudSat data at the time of our analysis. As CloudSat completes around 14.6 revolutions around Earth per day, there are around 5000 granules of observations annually in normal years like 2007–2010 and 2013–2016. In 2011–2012 and 2017–2019, the CloudSat observation was interrupted occasionally due to reasons such as battery anomalies or orbit maneuvers (https://cloudsat.atmos.colostate.edu/news/CloudSat_status), yielding fewer data in these years. Meanwhile, the granule amount is relatively larger in the boreal summer and autumn than in the winter and spring. This may imply that the data is less

representative of cloud climatology in the winter and spring seasons, but it does not affect the robustness of our scheme. It is shown below that the available data are more than enough for the scheme development and evaluation.

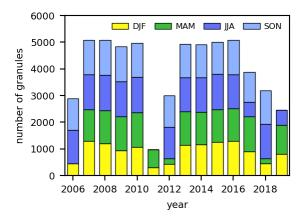


Figure 1. Year-by-year variation of CloudSat data amount used in this study. The colored segments indicate the portions of winter (December-January-February), spring (March-April-May), summer (June-July-August), and autumn (September-October-November), respectively.

2.2 Data preprocessing

Typical GCM grids have horizontal sizes (Δx) of 10–100s km (much larger than the CloudSat horizontal resolution) and vertical sizes (Δz) of 0.1–1s km (mostly larger than the CloudSat vertical resolution). Thus, the CloudSat clouds can be considered as sub-grid clouds at GCM grids, and the CloudSat data can be upscaled/aggregated to emulate atmospheric properties and cloud fraction simulated at GCM grids for the input and output of a cloud-fraction parameterization scheme.

In upscaling, the 'grid-mean' temperature, specific humidity, atmospheric pressure, and liquid/ice water contents are calculated by averaging the raw CloudSat data adjacent within the range of $\Delta x \times \Delta z$, while the sub-grid cloud fraction is calculated as the horizontal area cloud fraction (i.e., each profile in the cloudy subarea must have one or more of the 240-m layers with CPR cloud mask ≥ 30 within $\Delta x \times \Delta z$). The definition of sub-grid cloud fraction is consistent with that in most radiation parameterizations, and the resulting values are usually larger than the volume cloud fraction required by certain microphysical parameterizations (Grundner et al., 2022). More details of the upscaling process can be found in Wang et al. (2023). In addition, to account for the different horizontal and vertical resolutions of GCMs, the upscaling is carried out for 42 different Δx - Δz combinations. Therein, Δx spans 40–100 km with an increment of 10 km while Δz spans 10–60 hPa with an increment of 10 hPa, covering most grid sizes that may be seen in current GCMs.

It is noticed that the amount of available CloudSat data is far more than enough for the scheme development. For example, upscaling the data in 2015 to the resolution of $100 \text{ km} \times 20 \text{ hPa}$ (hereafter x100z20 for short) can yield more than 10 million cloudy samples, which is more than sufficient for training a neural network with only 100s trainable parameters (see Section 3.1). Therefore, to save training time, we randomly draw 100 granules from the data in 2015 when upscaling to each set of resolutions. The choice of 2015 is arbitrary and using the data in any other

year or multiple years does not affect the training results. Upscaling to 42 sets of resolutions yields more than 10 million cloudy samples in total. These samples are randomly split into three parts: 60% for scheme training, 20% for scheme validation, and 20% for scheme testing.

2.3 Data uncertainty

The CloudSat data uncertainty exists in two aspects. First, the uncertainty of satellite data retrieval has been discussed in previous studies (e.g., Weisz et al., 2007; Kotarba & Solecki, 2021). Notably, the radar-only product of 2B-GEOPROF (2B-CWC-RO) is less reliable for cloud mask (cloud water contents) than the radar-lidar (radar-visible) combined product of 2B-GEOPROF-Lidar (2B-CWC-RO), respectively. Here, we intentionally avoid using the latter two products to ensure the data inherent consistency to the most degree. The radar-lidar combined cloud mask is not consistent with cloud water contents in 2B-CWC-RO while the radar-visible combined water contents are only available for the daytime and thus less representative.

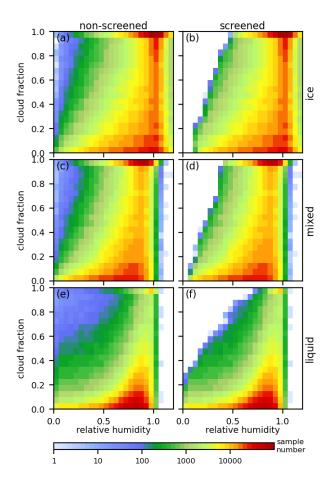


Figure 2. Effect of the isolation-forest screening on the data population. The shadings indicate sample numbers in the upscaled CloudSat data at the resolution of x100z20 for the whole year of 2015. An isolation-forest model is trained for clouds of each phase (i.e., ice, mixed, and liquid).

The inputs of the models are the relative humidity of the respective phases and the sub-grid cloud fraction, and the contamination ratio is set to 0.01.

Second, the uncertainty of atmospheric states from the ECMWF-AUX is remarkable but seldom discussed. Particularly, it was revealed that the upscaled CloudSat data have some anomalous samples with large cloud cover at very-low relative humidity (Wang et al., 2023), which is counterintuitive and unrealistic. These are attributed to biases in the ECMWF-AUX data. For example, the ECMWF model tends to underestimate the inversion layer height in the eastern subtropical ocean (e.g., the southeast Pacific, Andrejczuk et al., 2012; Chen et al., 2015; Chen and Wang, 2016a), causing underestimated relative humidity in the upper cloud layer. As there is not a well-defined quantitative relationship between the sub-grid cloud fraction and the gridmean relative humidity, it is difficult to find a physical-based method to detect these anomalous data.

Therefore, to facilitate the process of detecting anomalous samples in the upscaled data, we used an off-the-shelf machine-learning method—isolation forest (Liu et al., 2008, 2012). The method assumes that anomalous samples are isolatedly distributed from normal samples in the sample space and thus easier to be isolated than normal samples through random partitioning of the data. The algorithm builds a collection of binary trees from random subsets of data, where the anomalous samples should lead to shorter paths to leaves than normal samples, and aggregates the anomaly score from each tree to come up with a final anomaly score for determining the anomalous samples.

In this study, we train an isolation-forest model for clouds of each phase (i.e., ice, mixed-phase, and liquid) using 100,000 samples randomly drawn from the CloudSat data upscaled at the resolution of x100z20 for the whole year of 2015. The inputs for the models are sub-grid cloud fraction and relative humidity for the respective phases, where the saturated water vapor mixing ratio for the mixed phase is set to the weighted mean of those over ice and liquid surfaces. The contamination ratio, a parameter setting the proportion of anomalous samples in the dataset, is set to 0.01 for clouds of all three phases.

Figure 2 compares the sample number distributions of the non-screened and screened datasets. The anomalous samples exist in clouds of all three phases (Figs. 2a, 2c, and 2e). The screening only removes samples with large cloud fraction but small relative humidity and does not affect the rest samples (Figs. 2b, 2d, and 2f).

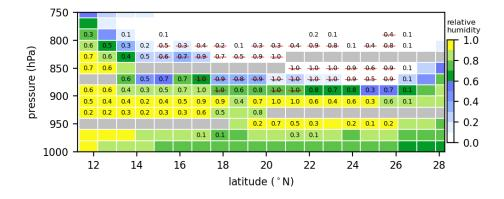


Figure 3. Effect of the data screening on data samples, demonstrated using the CloudSat observation at 12°–28°N by the granule No. 03307 on 11 December 2018, upscaled at x100z20. Numbers in the figure indicate observed sub-grid cloud fraction, colored shadings indicate relative humidity over the liquid surface, and grey shadings indicate no valid observations. The detected anomalous samples are marked with red strikethroughs.

To further demonstrate the effect of screening, we examine an example of the upscaled CloudSat observation by the granule No. 03307. Shown in Fig. 3, many samples in the upper portion of the cloud layer have the sub-grid cloud fraction (numbers in the figure) larger than 0.5 and the relative humidity (colored shadings in the figure) lower than 0.2, and the screening successfully distinguishes these anomalous samples (marked with red strikethroughs).

Note that the data screening is only to remove samples that we consider to be unrealistic. The data screening certainly does not affect the resulting scheme simply because the anomalous samples take a very small fraction of the CloudSat data (Fig. 2). Likewise, increasing the contamination ratio also has little effect on the scheme results over the normal samples that dominate the data population. For example, setting the contamination ratio to 0.05 further reduces the number of samples having large cloud fraction at small relative humidity but does not cause any evident changes to the variation of cloud fraction with either relative humidity or cloud condensate mixing ratio (shown in Figs. S1–S2 in the Supplementary Materials).

3 Scheme description

This section describes the neural network architecture and the algorithm of the Xu-Randall scheme. The database is the upscaled CloudSat data for 42 sets of resolutions (Section 2.2). The training, validation, and testing datasets include around 5.4, 1.8, and 1.8 million samples, respectively. The former two datasets are used for the NSA scheme development and the Xu-Randall scheme tuning, while the testing dataset is used for the scheme testing in Section 4.

3.1 Architecture of the network-based scale-adaptive cloud-fraction scheme

Figure 4 presents the architecture of the network-based scale-adaptive (NSA for short) cloud-fraction scheme (Fig. 4a). The network is composed of one input layer, a tunable number n of hidden layers, one output layer, and the ReLU activation layers (not shown in the figure) following the input layer and hidden layers. The loss function is the mean square error.

The input layer consists of 8 variables: air pressure (P), air temperature (T), liquid/ice water mixing ratios (Q_L/Q_I), relative humidity over liquid/ice surfaces (R_L/R_I , calculated with the upscaled atmospheric pressure, temperature, and specific humidity), and the horizontal/vertical grid sizes ($\Delta x/\Delta z$) of the host GCM. Therein, the first 6 variables are chosen because of their close association with cloud formation based on domain knowledge. They are also used in the Xu-Randall scheme, making it fair to compare results from the NSA and the Xu-Randall schemes in the following sections. Δx and Δz are to implicitly include the effects of grid sizes on the sub-grid cloud 3D structure (e.g., cloud sizes and vertical overlap) and thus the sub-grid cloud cover. As shown below, it provides the scheme with the flexibility of use at a variety of GCM resolutions.

We are aware that the input size could be reduced by replacing R_L and R_I using the specific humidity (Q_V) . However, using Q_V causes a larger burden for the neural network, and the resulting network should have more hidden layers or more neurons to get training accuracy close to that of the network using R_L and R_I . Thus, using R_L and R_I is a choice out of computation efficiency. The output layer has only one neuron, i.e., the sub-grid cloud fraction (CF).

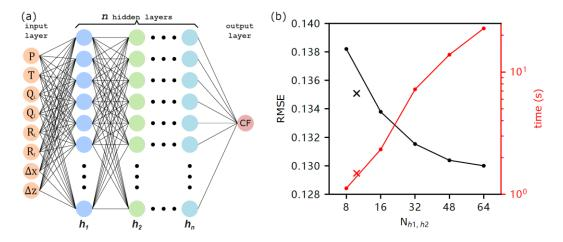


Figure 4. Architecture of the network-based scale-adaptive (NSA) cloud-fraction parameterization (a) and the variation of scheme performance with the neuron amounts in hidden layers for the four-layer version of the scheme (b). In (b), the black symbols and curve (with respect to the left y axis) give the root mean square error (RMSE) estimated on the validation dataset, while the red symbols and curve (with respect to the right y axis) give the time consumption of the network-based scheme, where the scheme is implemented in Fortran, compiled with the GNU Fortran compiler (i.e., gfortran), and executed for 3,000,000 times; and the cross symbols indicate results of the NSA scheme with 10 neurons in both hidden layers. There are 211 trainable parameters in the cross-signed scheme. The output of the network is bounded to 0–1 before the analysis.

The number of hidden layers (n) and the neuron amounts in each hidden layer (N_{hi} , i = 1, 2, ..., n) are tunable hyperparameters in the network. Unlike most deep-learning studies that determine the hyperparameters based on only the validation accuracy, this study takes a compromise between the validation accuracy and the computational efficiency, as the scheme is planned to be executed every time step at each grid of the host GCM. As shown in Fig 4b, when n equals 2, the validation root-mean-square error (RMSE) decreases by about 6% as $N_{hI,h2}$ increases from 8 to 64, while the time consumption increases by more than 20 times. Clearly the computational efficiency is not an ignorable factor. In addition, using one hidden layer increases the RMSE too much, while using three hidden layers leads to lower computation efficiency. Therefore in this study, we set n to 2, N_{hI} and N_{h2} both to 10. This setting yields a validation RMSE of 0.135 (black cross) and a time consumption of 1.48 s for 3,000,000 executions (red cross), which is about 5 times that of the Xu-Randall scheme and still acceptable. Below, the scheme testing and the offline application of the NSA scheme are both based on this setting.

We utilize one single network to parameterize the CF of different phases for simplicity. As the CF variation with Q_C and relative humidity is sensitive to the cloud phase (Wang et al.,

2023; also shown below in Fig. 6), using separate networks for clouds of different phases can yield better results. However, using multiple networks increases the memory cost for storing the network parameters and reduces the computational efficiency. Thus, the multiple-network approach is not taken in this study.

3.2 Tuned Xu-Randall scheme

The Xu-Randall scheme is a conventional diagnostic cloud-fraction parameterization scheme for use in climate models. It is the default cloud-fraction scheme in the Weather Research and Forecast (WRF) Model and has been used in many weather and climate studies (e.g., Chen et al., 2018b, 2021; Yang et al., 2018; Song et al., 2019). The scheme is also employed in the FGOALS-f3 GCM developed by the Institute of Atmospheric Physics, Chinese Academy of Sciences (Zhou et al., 2015). Therefore, this scheme is used as a baseline for evaluating the NSA scheme. Below we briefly introduce the Xu-Randall scheme, and more details can be found in the paper by Xu & Randall (1996).

The Xu-Randall scheme was built based on the simulations of a cloud ensemble model using a curve-fitting approach. It assumes the sub-grid cloud fraction is a function of the grid-mean relative humidity (R) and cloud condensate mixing ratio (Q_C , i.e., Q_I for ice clouds, Q_L for liquid clouds, and $Q_I + Q_L$ for mixed-phase clouds). The function formula is

$$CF = R^{\beta} \left[1 - \exp\left(-\frac{\alpha Q_C}{\left[(1 - R) Q^* \right]^{\gamma}} \right) \right], \text{ if } R < 1$$
 (1),

$$CF = 1$$
, if $R \ge 1$ (2),

where Q^* is the grid-mean water vapor saturation mixing ratio, $\alpha = 100$, $\beta = 0.25$, and $\gamma = 0.49$ are empirical parameters determined through curve-fitting based on the simulation dataset.

As the Xu-Randall scheme was built on a completely different dataset than the NSA scheme, it would be unfair to expect the scheme produces results close to the CloudSat observations. Therefore, we have tuned the scheme using the same procedure and the same datasets (i.e., the aforementioned training and validation datasets) that are used for training the NSA scheme, yielding $\alpha=70.3378$, $\beta=0.0507$, and $\gamma=0.6315$. Below we mainly present results from the tuned Xu-Randall scheme, and results of the original Xu-Randall scheme are also included in the Supplementary Materials for interested readers.

4. Scheme testing

This section evaluates the NSA scheme using the testing dataset within the context of a machine-learning study. Results of the cloud spatial and temporal characteristics predicted by the scheme are given in Section 5.

4.1 Accuracy

Figure 5 presents the joint probability density distribution of CFs from the scheme predictions and the CloudSat observations for clouds of different phases, estimated based on the

testing dataset. The NSA scheme is shown to well predict CFs for clouds of all three phases and has relatively larger biases (underestimation) when the observed CF is close to 1 (Figs. 5a, 5c, 5e). This could suggest the effect of the data imbalance. However, we found that balancing the CF frequency distribution by undersampling the training data could not much improve the results. This implies that the large-CF samples may have larger uncertainties or larger inherent inconsistencies, making the scheme difficult to learn.

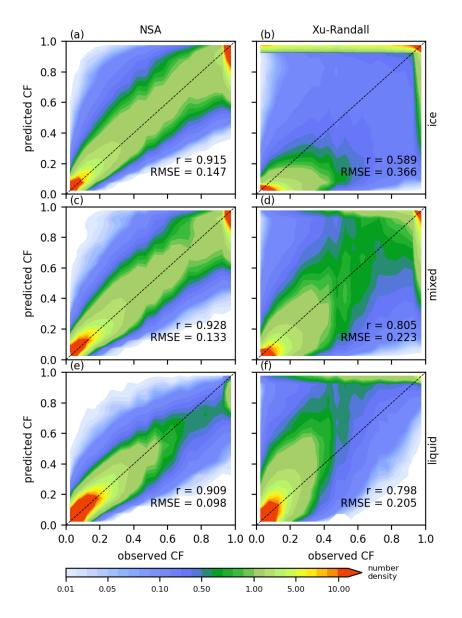


Figure 5. Joint probability density distribution between cloud fractions from the scheme predictions and the CloudSat observations for clouds of different phases (ice-only, mixed, and liquid-only), estimated based on the testing dataset: (left) results from the NSA scheme; and (right) results from the tuned Xu-Randall scheme. The lower-right numbers indicate the

correlation coefficient (*r*) and RMSE of the predictions with respect to the observations for each type of clouds.

It is noticed that the correlation coefficient (r, larger is better) is the largest for the mixed-phase clouds, while the RMSE (smaller is better) is the smallest for the liquid clouds. The two metrics are not consistent for two reasons. First, the fraction of large-CF samples is much larger in ice and mixed-phase clouds than in liquid clouds. Large-CF samples contribute more to the RMSE than small-CF samples, causing the relatively larger RMSE in ice and mixed-phase clouds. Second, the CloudSat data for liquid clouds might have large uncertainties. Liquid clouds are mostly sited in the lower troposphere, where the atmospheric properties are dominated by turbulence and difficult to simulate by GCMs. Therefore, air temperature and humidity from the ECMWF-AUX may have large uncertainties in the lower troposphere, causing the smaller r for the CF prediction of liquid clouds.

In contrast, the tuned Xu-Randall scheme yields larger RMSE and smaller correlation coefficient for clouds of all three phases. The biases over ice clouds are the largest, where the RMSE is 0.366, more than twice that of the NSA scheme, and the correlation coefficient is less than 0.6. It is noticed that the original Xu-Randall scheme reaches better results over the liquid clouds but worse results over the mixed and ice clouds (shown in Fig. S3) than the tuned one. This indicates the tuning process has opposite effects on the scheme performance over liquid vs. mixed and ice clouds and suggests that the sub-grid statistics could be sensitive to the cloud phases. Moreover, even when we tune the scheme individually for each upscaled resolution, the scheme still exhibits obvious inferiorities to the NSA scheme at all resolutions (shown in Fig. S4).

Figure 6 shows the variation of cloud fraction with relative humidity and cloud condensate mixing ratio from the CloudSat observations and the scheme predictions. In the observations, the ice CF is dominated by R (Fig. 6a), the liquid CF is dominated by Q_C (Fig. 6i), and the mixed CF is sensitive to both factors (Fig. 6e). It is worth highlighting that holding Q_C unchanged, the CF variation with R is non-monotonic for clouds of all three phases. The liquid CF decreases with R until R equals around 0.8, and increases afterward. In contrast, the ice CF increases with R until R equals around 1, and decreases afterward. The mixed CF exhibits a complex pattern perhaps due to the phase partition of Q_C . It is also noticed that the supersaturation (i.e., R > 1), which seldom occurs in liquid clouds, is not infrequent in ice clouds.

The NSA scheme prediction presents patterns quite close to the observed ones. Particularly, the scheme well captures the non-monotonic feature of the CF variation with R. For samples that dominate the data population (i.e., samples below the black contours), the scheme results are almost identical to the observations. The scheme may underestimate CF when Q_C is large (especially for ice and mixed-phase clouds, Fig. 6a vs. Fig. 6b, Fig. 6e vs. Fig. 6f). Nevertheless, the occurrence frequency of the associated samples (i.e., samples above the black contours in Figs. 6d, 6h, and 6l) is very low.

The tuned Xu-Randall scheme prediction presents similar patterns for clouds of three phases, in line with the same formula (i.e., Eqs. 1–2) across different cloud phases. The patterns for liquid and mixed clouds (Figs. 6g and 6k) are close to the CloudSat observations, consistent with the relatively larger correlation coefficients and smaller RMSEs in Figs. 5d and 5f. However, the pattern for ice clouds (Fig. 6c) is quite different from the observed one, showing

the scheme underestimates CF for Q_C < 50 mg kg⁻¹ and overestimates CF for R > 1. Results for the original Xu-Randall scheme are similar to the tuned one (figure not shown). Neither the original nor the tuned Xu-Randall scheme can capture the non-monotonic variation of CF with R, which is not included in the parameterization formula.

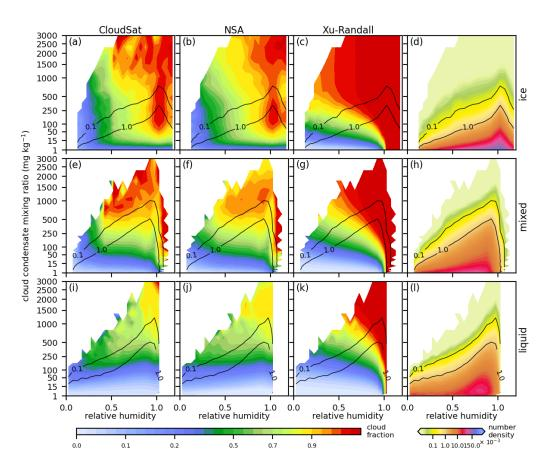


Figure 6. Comparisons of cloud fraction as a function of cloud condensate mixing ratio and relative humidity between the CloudSat observations (a, e, i), the NSA scheme (b, f, j), and the tuned Xu-Randall scheme (c, g, k) for clouds of different phases (ice-only, mixed, and liquid only), estimated based on the testing dataset. The right column (d, h, l) indicates the joint probability density distribution of respective cloud types in the testing dataset. Black lines indicate contours of the probability density of 0.001 and 0.0001, below which lie more than 88% and 97% of the corresponding sample populations, respectively.

4.2 Scale adaptivity

To examine whether considering Δx and Δz improves the NSA scheme performance, we take two additional network-based schemes as baselines: N and Nx100z20. Both schemes have the same network architecture as the NSA scheme except for excluding Δx and Δz from the input layer. The N scheme is trained based on the same dataset as the NSA scheme, while the Nx100z20 is trained based on the upscaled CloudSat at the resolution of x100z20 for the whole year of 2015 (no random drawing), where the sample amount is similar to that of the database for

training the NSA scheme. Below we compare the three network-based schemes based on the same testing dataset that is used above in Figs. 5–6.

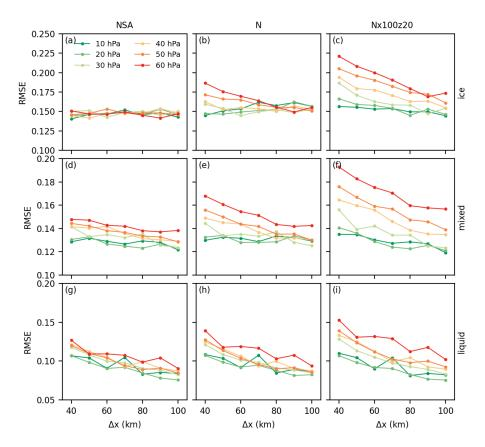


Figure 7. Comparisons of RMSE at different horizontal and vertical resolutions between the predictions of three neural network-based schemes estimated based on the testing dataset. Both N and Nx100z20 schemes have identical architecture to the NSA scheme except for excluding Δx and Δz from the input layer. The N scheme is trained with the same database as the NSA scheme, while the Nx100z20 scheme is trained based on the upscaled CloudSat data at the resolution of x100z20 for the whole year of 2015.

Figure 7 compares the RMSE of the three network-based schemes for samples with different horizontal and vertical resolutions. In the NSA scheme, the RMSE is not sensitive to Δx or Δz for ice clouds (Fig. 7a), slightly sensitive to Δz for mixed clouds (Fig. 7d), and sensitive to both resolutions for liquid clouds (Fig. 7g), where the RMSE tends to increase with Δz and decreases with Δx . When Δx and Δz are excluded from the input layer, the N scheme has larger RMSEs for clouds of all three phases, especially the ice and mixed clouds (Figs. 7b, 7e). As the deficiency of the N scheme may be attributed to the inherent inconsistency of the training database associated with different resolutions, we further examine the results of the Nx100z20, where the database inherent consistency is warranted. However, it shows that the RMSEs of the Nx100z20 scheme are even larger (Figs. 7c, 7f, 7i), and close to those of the NSA scheme only when Δx is the largest and Δz is the smallest. Therefore, we can conclude that both horizontal

and vertical resolutions affect the sub-grid statistics of cloud fraction, and that including Δx and Δz in the scheme greatly increases the scale adaptivity of the NSA scheme, leading to higher robustness for use in GCMs with different horizontal and vertical resolutions.

Figure 8 presents the mean cloud fraction at different horizontal and vertical resolutions from the CloudSat observations and the scheme predictions to show more details of how Δx and Δz may affect the cloud fraction parameterization. In the CloudSat observations (Figs. 8a, 8e, and 8i), the cloud fraction tends to increase with Δz and decrease with Δx . The NSA scheme well captures this feature, and the biases are less than 0.01 at most resolutions (Figs. 8b, 8f, and 8j). In contrast, the biases of the N scheme are larger than 0.01 for most resolutions and can have values up to 0.09). Meanwhile, the biases are generally symmetric about the diagonal, i.e., negative in the upper left and positive in the lower right. This is not a surprise. The scheme does not consider the resolution variability in the training database, and consequently the scheme biases tend to be the smallest in the middle of the resolution ranges and increase when the resolutions go toward either end. When we remove the inherent inconsistency associated with resolutions from the training database, the Nx100z20 scheme only shows better performance for samples with resolutions close to x100z20 (i.e., Δx in 80–100 km and Δz in 10–20 hPa). The bias increases rapidly with the decrease of Δx and the increase of Δz , with the largest value of 0.14. Hence, it is further confirmed that the NSA scheme has good scale adaptivity.

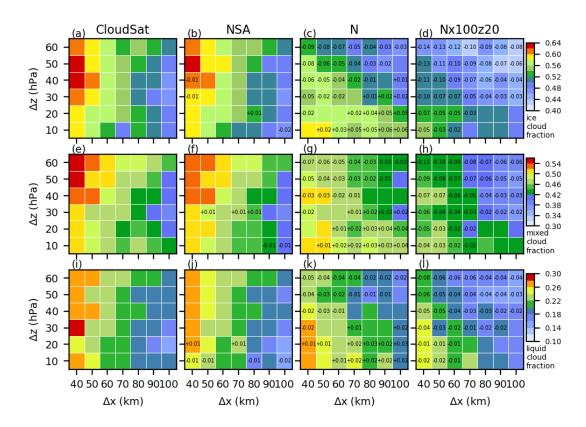


Figure 8. Comparisons of mean cloud fraction at different horizontal (Δx) and vertical (Δz) resolutions between the CloudSat observations and the predictions of three neural network-based

schemes, estimated based on the testing dataset. The numbers indicate the prediction-observation differences (prediction minus observation) with absolute values larger than 0.01.

5 Offline application

This section compares the climatology of cloud spatial and temporal variability simulated by the NSA scheme with those from the CloudSat observations and the tuned Xu-Randall scheme using an offline method. The NSA and the tuned Xu-Randall schemes both take the upscaled CloudSat data at the resolution of x100z20 for the period of 2006–2019 as inputs to make the respective predictions. We first get an intuitive understanding of the scheme biases (Fig. 9), then examine the generalizability of the NSA scheme (Fig. 10), and last assess the scheme performance based on 2006–2019 multiple-year mean results (Figs. 11–13).

We take the offline mode rather than incorporating the two schemes into a host model to exclude the distractions that could be caused by other model components (e.g., the simulated cloud condensate mixing ratios in the host model may deviate too much from the observations, Jiang et al., 2012) and possible feedbacks. Hence, the scheme-observation discrepancies can be mostly attributed to the scheme deficiencies, and the inter-scheme differences are not blurred by the possible compensating biases within the host model.

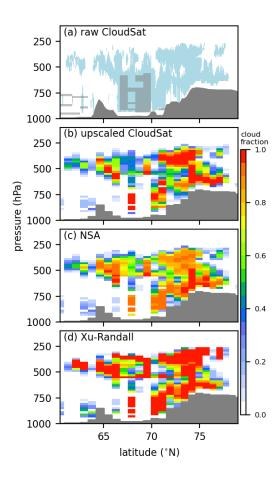


Figure 9. CloudSat observed cloud fraction at 60°-79°N by the granule No. 66364 on 13 October 2018 (a–b) compared with those from the NSA (c) and the tuned Xu-Randall (d) schemes. The dark gray regions at lower levels indicate the surface terrain. In (a), the light blue indicates overcast cloud coverage (CPR cloud mask equals 30 or 40), in which the light-gray regions are grids where the CloudSat does not have a valid observation for one or more of gridmean properties that are required for parameterizing the sub-grid cloud fraction.

Figure 9 presents the observed and modeled cloud fractions in a CloudSat granule to get a better understanding of the data upscaling and an intuitive view of the scheme biases. In the raw CloudSat data (Fig. 9a), a binary CF is determined by the CPR cloud mask: 1 for CPR cloud mask \geq 30 and 0 otherwise. When upscaled (Fig. 9b), the sub-grid CF has decimal values within 0–1. The upscaled CF may not have valid values at certain grids (indicated by light grey in Fig. 8a) due to two reasons. First, the raw CloudSat does not have valid estimates for liquid or ice cloud water content; and second, none of the raw CloudSat data falls in the range of Δz because the pressure change in 240 m exceeds Δz (this situation occurs mainly in the lower atmosphere where the vertical gradient of atmospheric pressure is large).

The NSA and the tuned Xu-Randall schemes both well predict the general distribution of the sub-grid CF (Figs. 9c–d) but exhibit different characteristics in the scheme-observation discrepancies. The NSA scheme tends to underestimate CF when CF is close to 1 (consistent with results in Figs. 5–6), while the Xu-Randall scheme overestimates CF at many grids (particularly the high-level CF that are mostly ice clouds) because of its treatment of CF at supersaturation. The Xu-Randall scheme assumes that CF equals 1 when the grid-mean RH equals or exceeds 1 (Eq. 2). This assumption works well for liquid clouds where the supersaturation is usually very low (Fig. 6l), but not for ice clouds where the occurrence of large supersaturation is not scarce (Fig. 6d).

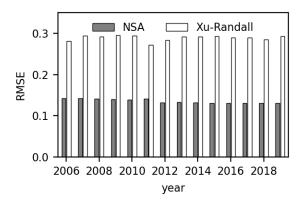


Figure 10. Cloud-fraction RMSE year-by-year variation of the NSA and the tuned Xu-Randall scheme predictions with respect to the CloudSat observations. Only cloudy grids are included in the calculation.

Figure 10 gives the year-by-year variation of the cloud-fraction RMSE, calculated with cloudy samples of all phases. Despite that the schemes are trained/tuned based on only data from

the year of 2015, the year-by-year variations of both RMSEs are very small (both within the range of \pm 4% of the multiple-year mean) and do not show clear sensitivity to the interannual climate variability. Meanwhile, the RMSEs in 2011 (2006, 2012, and 2018), where the CloudSat data are dominated by granules in winter and spring (summer and autumn), present no unique features distinguished from results in other years. Therefore, it is inferred that the generalizability of the NSA scheme is very good and at least similar to that of the Xu-Randall scheme, warranting its robustness in different climates.

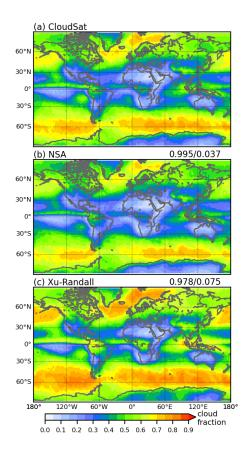


Figure 11. 2006–2019 mean global distribution of total cloud fraction (assuming maximum-random overlap) from the CloudSat observation, the NSA scheme, and the tuned Xu-Randall scheme. Numbers at the upper right corners of (b) and (c) indicate the correlation coefficient (*r*; before the slash) and RMSE (after the slash) of the respective scheme predictions with respect to the CloudSat observations. The global-mean total cloud fraction is 0.46, 0.42, and 0.52 for the CloudSat observations, the NSA, and the tuned Xu-Randall scheme predictions, respectively.

Figure 11 compares the 2006–2019 averaged global distributions of total CF from the observation and the scheme predictions, assuming the maximum-random overlap. The observed CF is larger in the tropics and the regions around 60° of both hemispheres and smaller in the subtropical regions. The two schemes both capture the general patterns. The tuned Xu-Randall prediction has a global mean of 0.52, larger than that from the original Xu-Randall scheme (0.46; Fig. S5a), which is closer to the observation (0.46) than the NSA prediction (0.42). However, the

original/tuned Xu-Randall prediction has too large CF over the tropics (especially the India-Pacific warm pool) and too small/large CF over the Southern Ocean, where the NSA prediction is closer to the observation. Consequently, the NSA prediction has a larger spatial correlation coefficient (0.995) and a smaller RMSE (0.037) than the Xu-Randall predictions. Using the maximum overlap assumption reaches similar results while using the random overlap suggests that the tuned Xu-Randall scheme prediction is closer to the observation (shown in Table S1 in the Supplementary Materials). These conflicting results imply that the cloud vertical structure could be quite different between the scheme predictions, as examined below.

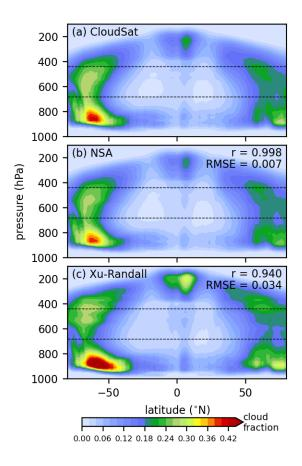


Figure 12. 2006–2019 averaged zonal-mean vertical distribution of cloud fraction from the CloudSat observations, the NSA and the tuned Xu-Randall scheme predictions. Numbers in (b) and (c) indicate the correlation coefficient (*r*) and RMSE of the respective scheme predictions with respect to the CloudSat observations. Dashed lines indicate the heights of 440 hPa and 680 hPa, respectively.

Figure 12 presents the zonal-mean vertical structure of CF from the observations and the scheme predictions. In the tuned Xu-Randall scheme, the CF overestimation in the tropics is associated with the too-large high-level CF (clouds above 440 hPa), while the CF overestimation in regions around 60°S and 60°N is due to the too-large low-level CF (clouds below 680 hPa). The original Xu-Randall scheme overestimates the high-level CF in the tropics as well but

underestimates the low-level CF in regions around 60°S and 60°N (Fig. S5b). The tuning causes larger CF at all levels and yields better mid-level CF but worse low-level CF, which is consistent with the results on mixed and liquid clouds shown in Fig. 5 and Fig. S3. The NSA scheme predicts smaller high-level CF in the tropics and smaller mid- and low-level CFs in regions around 60°S and 60°N and reaches a larger spatial correlation (0.998) and a smaller RMSE (0.007) than both the original and tuned Xu-Randall schemes.

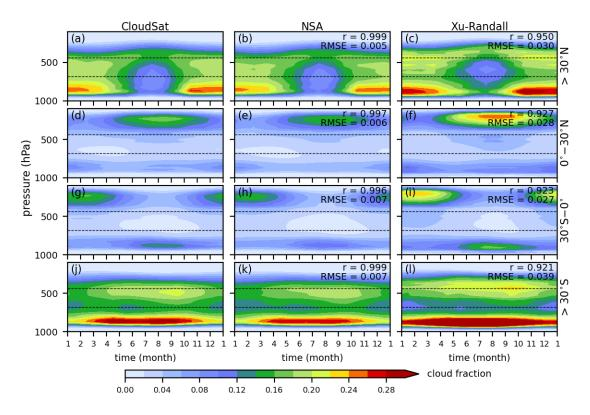


Figure 13. Annual variation of cloud vertical distribution averaged at different latitudes from the CloudSat observations (left), the NSA (middle), and the tuned Xu-Randall (right) scheme predictions. Numbers in middle and right columns indicate the correlation coefficient (*r*) and RMSE of the respective scheme predictions with respect to the CloudSat observations. Dashed lines indicate the heights of 440 hPa and 680 hPa, respectively.

Figure 13 further examines the seasonal variations of the cloud vertical structure at different latitudes. In the observations, the cloud vertical structure varies with the seasonal migration at all latitudes. While both schemes can predict the general variation, the NSA scheme shows better results (i.e., larger correlation coefficient and smaller RMSE) than the original (Fig. S6) and tuned Xu-Randall schemes in all seasons and all latitudes. This indicates that the NSA scheme generally exhibits superiorities in the spatial distribution of total CF and the cloud vertical structure, and further confirms that the superiorities are not sensitive to the spatio-temporal variability of the large-scale meteorology conditions, suggesting the scheme has enough robustness to simulate CF over different climate regimes.

6 Summary and discussion

This study presents a neural network-based cloud-fraction parameterization scheme for use in climate models. The scheme is developed using the CloudSat (quasi-)observational data, and for the first time considers explicitly the effects of both horizontal and vertical grid sizes on the cloud-fraction parameterization. It not only simulates realistically the cloud characteristics but also captures the observed non-monotonic functional relationship of cloud fraction with relative humidity. In addition, our preliminary study shows that using the network-based scheme in the WRF Model hardly increases the computation time as compared with using the Xu-Randall scheme. The utility of the scheme in GCMs shows promising features in accuracy, scale adaptivity, and computational efficiency.

In the case of comparing with the Xu-Randall parameterization, the network-based scheme simulates more-realistic total cloud fraction spatial distribution and cloud vertical structure. Particularly, the biases of too-large high-level cloud fraction over the tropics and too-small low-level cloud fraction over regions around 60°S and 60°N in the original Xu-Randall scheme, which agrees with the too-strong LWCRE and too-weak SWCRE over the respective regions as shown in current GCMs (Flato et al., 2013; Schuddeboom and McDonald, 2021; Chen et al., 2022), are much eased.

We are aware that the grid-mean atmospheric properties in GCMs could differ markedly from the CloudSat data (e.g., Jiang et al., 2012), hindering the above findings from being fully justified in GCMs. Hence, one of our undergoing studies is to further evaluate the NSA scheme using the ERA-Interim reanalysis (Dee et al., 2011), where the grid-mean relative humidity is quasi observed due to the assimilation while the cloud condensates are fully model simulated. The preliminary results show that although cloud condensate mixing ratios in the reanalysis are much smaller than the CloudSat observations, using the NSA scheme still yields better mid- and high-level cloud fractions than the original Xu-Randall scheme (figure not shown). Therefore, it is believed that incorporating the network-based scheme has great potential to improve the cloud radiative effects and the energy budget in GCMs.

One important aspect of cloud fraction is the vertical overlap, which has significant implications to cloud radiative effects (e.g., Liang & Wang, 1997; Zhang & Jing, 2016; Wang et al., 2021). As shown by Zhang et al. (2013), the inter-GCM spreads in cloud radiative effects can be largely attributed to the different treatments of cloud vertical overlap. In our scheme, this aspect, at least in the sub-grid scale, is implicitly considered, which reduces the simulation biases in cloud fraction (shown in Figs. 7–8). Therefore, further investigation of the grid-scale cloud vertical overlap using similar approaches is plausible and warranted.

Appendix

The root-mean square error (RMSE) and correlation coefficient (r) of a prediction with respect to the observation are calculated as follows:

$$RMSE = \sqrt{\sum_{i=1}^{M} \left(\operatorname{pred}_{i} - \operatorname{obs}_{i} \right)^{2} / M}$$
 (A1)

$$r = \frac{\sum_{i=1}^{M} \left(\operatorname{pred}_{i} - \overline{\operatorname{pred}} \right) \left(\operatorname{obs}_{i} - \overline{\operatorname{obs}} \right)}{\sqrt{\sum_{i=1}^{M} \left(\operatorname{pred}_{i} - \overline{\operatorname{pred}} \right)^{2}} \sqrt{\sum_{i=1}^{M} \left(\operatorname{obs}_{i} - \overline{\operatorname{obs}} \right)^{2}}}$$
(A2).

Therein, the pred and obs stand for the prediction and observation datasets, respectively, i for the sample index, and M for the sample amounts.

Open Research

The CloudSat data is available at https://www.cloudsat.cira.colostate.edu, and the code for the Xu-Randall scheme was obtained from the Weather Research Forecast Model Version 3.7.1 (https://www2.mmm.ucar.edu/wrf/users/download/get_source.html). The network was implemented using the Pytorch application programming interface (https://pytorch.org/). The codes for upscaling CloudSat data, scheme training, and result analysis together with the databases for training NSA and Nx100z20 schemes are preserved at https://doi.org/10.5281/zenodo.7539634.

Acknowledgments

This study is supported by the National Key R&D Program of China (2021YFC3000801) and the National Natural Science Foundation of China (42275074). WCW acknowledges the support from the SUNY Research Foundation Fixed-Price Balance Account (31972). The authors thank the editor (Dr. Tapio Schneider) and the two anomalous reviewers for their kind and patient comments, which greatly help clarify and improve this manuscript.

References

Andrejczuk, M., Grabowski, W. W., Gadian, A., & Burton, R. (2012). Limited-area modelling of stratocumulus over South-Eastern Pacific. *Atmospheric Chemistry and Physics*, *12*(7), 3511–3526. https://doi.org/10.5194/acp-12-3511-2012

- Austin, R. T., and Wood, N. B. (2018). Level 2B radar-only cloud water content (2B-CWC-RO) process description and interface control document, product version P1_R05. NASA JPL CloudSat project document revision 0., 51 pp. Available from https://www.cloudsat.cira.colostate.edu/cloudsat-static/info/dl/2b-cwc-ro/2B-CWC-RO_PDICD.P1_R05.rev0_.pdf.
- Bodas-Salcedo, A., Webb, M. J., Brooks, M. E., Ringer, M. A., Williams, K. D., Milton, S. F., & Wilson, D. R. (2008). Evaluating cloud systems in the Met Office global forecast model using simulated CloudSat radar reflectivities. *Journal of Geophysical Research*, *113*, D00A13. https://doi.org/10.1029/2007JD009620
- Caldwell, P. M., Zelinka, M. D., Taylor, K. E., & Marvel, K. (2016). Quantifying the sources of intermodel spread in equilibrium climate sensitivity. *Journal of Climate*, 29(2), 513–524. https://doi.org/10.1175/jcli-d-15-0352.1
- Chantry, M., Christensen, H., Dueben, P., & Palmer, T. (2021). Opportunities and challenges for machine learning in weather and climate modelling: hard, medium and soft AI. *Philosophical Transactions of the Royal Society A: Mathematical, Physical and Engineering Sciences*, 379(2194), 20200083. https://doi.org/10.1098/rsta.2020.0083
- Chen, G., & Wang, W.-C. (2016a). Aerosol–stratocumulus–radiation interactions over the southeast Pacific: Implications to the underlying air–sea coupling. *Journal of the Atmospheric Sciences*, 73(7), 2759–2771. https://doi.org/10.1175/JAS-D-15-0277.1
- Chen, G., & Wang, W.-C. (2016b). An effective approach to evaluate GCM simulated diurnal variation of clouds. *Geophysical Research Letters*, 43(20), 11064–11071. https://doi.org/10.1002/2016gl070446
- Chen, G., & Wang, W.-C. (2022). Short-term precipitation prediction for contiguous United States using deep learning. *Geophysical Research Letters*, 49(8). https://doi.org/10.1029/2022GL097904
- Chen, G., Wang, W.-C., & Chen, J.-P. (2015). Aerosol-stratocumulus-radiation interactions over the southeast Pacific. *Journal of the Atmospheric Sciences*, 72(7), 2612–2621. https://doi.org/10.1175/jas-d-14-0319.1
- Chen, G., Wang, W.-C., & Chen, J. P. (2018a). Circulation responses to regional aerosol climate forcing in summer over East Asia. *Climate Dynamics*, *51*(11), 3973–3984. https://doi.org/10.1007/s00382-018-4267-3
- Chen, G., Wang, W.-C., Cheng, C.-T., & Hsu, H.-H. (2021). Extreme snow events along the coast of the northeast United States: Potential changes due to global warming. *Journal of Climate*, *34*(6), 2337–2353. https://doi.org/10.1175/JCLI-D-20-0197.1
- Chen, G., Wang, W.-C., Bao, Q., & Li, J. (2022). Evaluation of simulated cloud diurnal variation in CMIP6 climate models. *Journal of Geophysical Research: Atmospheres*, 127(6). https://doi.org/10.1029/2021JD036422
- Chen, G., Xue, H., Feingold, G., & Zhou, X. (2012a). Vertical transport of pollutants by shallow cumuli from large eddy simulations. *Atmospheric Chemistry and Physics*, *12*(23), 11319–11327. https://doi.org/10.5194/acp-12-11319-2012

- Chen, G., Yang, J., Bao, Q., & Wang, W.-C. (2018b). Intraseasonal responses of the East Asia summer rainfall to anthropogenic aerosol climate forcing. *Climate Dynamics*, *51*(11), 3985–3998. https://doi.org/10.1007/s00382-017-3691-0
- Chen, T., Guo, J., Li, Z., Zhao, C., Liu, H., Cribb, M., et al. (2016). A CloudSat perspective on the cloud climatology and its association with aerosol perturbations in the vertical over eastern China. *Journal of the Atmospheric Sciences*, 73(9), 3599–3616. https://doi.org/10.1175/jas-d-15-0309.1
- Dee, D. P., Uppala, S. M., Simmons, A. J., Berrisford, P., Poli, P., Kobayashi, S., et al. (2011). The ERA-Interim reanalysis: configuration and performance of the data assimilation system. *Quarterly Journal of the Royal Meteorological Society*, *137*(656), 553–597. https://doi.org/10.1002/qj.828
- Di Giuseppe, F., & Tompkins, A. M. (2015). Generalizing cloud overlap treatment to include the effect of wind shear. *Journal of the Atmospheric Sciences*, 72(8), 2865–2876. https://doi.org/10.1175/jas-d-14-0277.1
- Flato, G., Marotzke, J., Abiodun, B., Braconnot, P., Chou, S. C., Collins, W., et al. (2013). Evaluation of Climate Models. In T. F. Stocker, D. Qin, G.-K. Plattner, M. Tignor, S. K. Allen, J. Boschung, et al. (Eds.), *Climate Change 2013: The Physical Science Basis. Contribution of Working Group I to the Fifth Assessment Report of the Intergovernmental Panel on Climate Change* (pp. 741–866). Cambridge, United Kingdom and New York, USA: Cambridge University Press.
- Greenwald, T. J., Lee, Y.-K., Otkin, J. A., & L'Ecuyer, T. (2010). Evaluation of midlatitude clouds in a largescale highresolution simulation using CloudSat observations. *Journal of Geophysical Research: Atmospheres*, 115, D19203. https://doi.org/10.1029/2009JD013552.
- Grundner, A., Beucler, T., Gentine, P., Iglesias-Suarez, F., Giorgetta, M. A., & Eyring, V. (2022). Deep learning based cloud cover parameterization for ICON. *Journal of Advances in Modeling Earth Systems*, *14*(12). https://doi.org/10.1029/2021MS002959
- Ham, Y.-G., Kim, J.-H., & Luo, J.-J. (2019). Deep learning for multi-year ENSO forecasts. *Nature*, *573*(7775), 568–572. https://doi.org/10.1038/s41586-019-1559-7
- Han, Y., Zhang, G. J., Huang, X., & Wang, Y. (2020). A moist physics parameterization based on deep learning. *Journal of Advances in Modeling Earth Systems*, *12*(9). https://doi.org/10.1029/2020MS002076
- Jiang, J. H., Su, H., Zhai, C., Perun, V. S., Del Genio, A., Nazarenko, L. S., et al. (2012). Evaluation of cloud and water vapor simulations in CMIP5 climate models using NASA "A-Train" satellite observations. *Journal of Geophysical Research: Atmospheres*, 117(D14), D14105. https://doi.org/10.1029/2011JD017237
- Kato, S., Sun-Mack, S., Miller, W. F., Rose, F. G., Chen, Y., Minnis, P., & Wielicki, B. A. (2010). Relationships among cloud occurrence frequency, overlap, and effective thickness derived from CALIPSO and CloudSat merged cloud vertical profiles. *Journal of Geophysical Research: Atmospheres*, 115(D4), D00H28. https://doi.org/10.1029/2009jd012277

- Kim, H., Ham, Y. G., Joo, Y. S., & Son, S. W. (2021). Deep learning for bias correction of MJO prediction. *Nature Communications*, *12*(1), 3087. https://doi.org/10.1038/s41467-021-23406-3
- Kodama, C., Noda, A. T., & Satoh, M. (2012). An assessment of the cloud signals simulated by NICAM using ISCCP, CALIPSO, and CloudSat satellite simulators: Assessment of cloud simulated by NICAM. *Journal of Geophysical Research: Atmospheres*, 117(D12), n/a-n/a. https://doi.org/10.1029/2011JD017317
- Kotarba, A.Z., Solecki, M., 2021. Uncertainty assessment of the vertically-resolved cloud amount for joint CloudSat–CALIPSO radar–lidar observations. Remote Sensing 13, 807. https://doi.org/10.3390/rs13040807
- Krasnopolsky, V. M., & Fox-Rabinovitz, M. S. (2006). Complex hybrid models combining deterministic and machine learning components for numerical climate modeling and weather prediction. *Earth Sciences and Environmental Applications of Computational Intelligence*, 19(2), 122–134. https://doi.org/10.1016/j.neunet.2006.01.002
- Leinonen, J., Nerini, D., & Berne, A. (2021). Stochastic super-resolution for downscaling time-evolving atmospheric fields with a generative adversarial network. *IEEE Transactions on Geoscience and Remote Sensing*, 59(9), 7211–7223. https://doi.org/10.1109/TGRS.2020.3032790
- Lau, K. M., Kim, M. K., & Kim, K. M. (2006). Asian summer monsoon anomalies induced by aerosol direct forcing: The role of the Tibetan Plateau. *Climate Dynamics*, 26(7–8), 855–864. https://doi.org/10.1007/s00382-006-0114-z
- Li, J., Lv, Q., Jian, B., Zhang, M., Zhao, C., Fu, Q., et al. (2018). The impact of atmospheric stability and wind shear on vertical cloud overlap over the Tibetan Plateau. *Atmospheric Chemistry and Physics*, 18(10), 7329–7343. https://doi.org/10.5194/acp-18-7329-2018
- Li, J., Sun, Z., Liu, Y., You, Q., Chen, G., & Bao, Q. (2021). Top-of-atmosphere radiation budget and cloud radiative effects over the Tibetan plateau and adjacent monsoon regions from CMIP6 simulations. *Journal of Geophysical Research: Atmospheres*, *126*(9), e2020JD034345. https://doi.org/10.1029/2020JD034345
- Liang, X. Z., & Wang, W. C. (1997). Cloud overlap effects on general circulation model climate simulations. *Journal of Geophysical Research-Atmospheres*, *102*(D10), 11039–11047.
- Liu, F. T., Ting, K. M., & Zhou, Z.-H. (2008). Isolation Forest. In *Eighth IEEE International Conference on Data Mining* (pp. 413–422).
- Liu, F. T., Ting, K. M., & Zhou, Z.-H. (2012). Isolation-based anomaly detection. *ACM Trans. Knowl. Discov. Data*, 6(1). https://doi.org/10.1145/2133360.2133363
- Marchand, R., Mace, G. G., Ackerman, T., & Stephens, G. (2008). Hydrometeor detection using CloudSat—An Earth-orbiting 94-GHz cloud radar. *Journal of Atmospheric and Oceanic Technology*, 25(4), 519–533. https://doi.org/10.1175/2007JTECHA1006.1
- Nooteboom, P. D., Feng, Q. Y., López, C., Hernández-García, E., & Dijkstra, H. A. (2018). Using network theory and machine learning to predict El Niño. *Earth Syst. Dynam.*, *9*(3), 969–983. https://doi.org/10.5194/esd-9-969-2018

- Pan, B., Hsu, K., AghaKouchak, A., & Sorooshian, S. (2019). Improving Precipitation Estimation Using Convolutional Neural Network. *Water Resources Research*, *55*(3), 2301–2321. https://doi.org/10.1029/2018WR024090
- Pan, B., Anderson, G. J., Goncalves, A., Lucas, D. D., Bonfils, C. J. W., Lee, J., et al. (2021). Learning to Correct Climate Projection Biases. *Journal of Advances in Modeling Earth Systems*, *13*(10). https://doi.org/10.1029/2021MS002509
- Pan, B., Anderson, G. J., Goncalves, A., Lucas, D. D., Bonfils, C. J. W., & Lee, J. (2022). Improving seasonal forecast using probabilistic deep learning. *Journal of Advances in Modeling Earth Systems*, *n/a*(n/a), e2021MS002766. https://doi.org/10.1029/2021MS002766
- Park, R.-S., Chae, J.-H., & Hong, S.-Y. (2016). A revised prognostic cloud fraction scheme in a global forecasting system. *Monthly Weather Review*, *144*(3), 1219–1229. https://doi.org/10.1175/MWR-D-15-0273.1
- Partain, P. (2022). CloudSat ECMWF-AUX auxillary data product process description and interface control document, product version P1_R05. NASA JPL CloudSat project document revision 0., 16 pp. Available from https://www.cloudsat.cira.colostate.edu/cloudsat-static/info/dl/ecmwf-aux/ECMWF-AUX.PDICD.P1_R05.rev0.pdf.
- Rasp, S., & Lerch, S. (2018). Neural networks for postprocessing ensemble weather forecasts. *Monthly Weather Review*, *146*(11), 3885–3900. https://doi.org/10.1175/MWR-D-18-0187.1
- Rasp, S., Pritchard, M. S., & Gentine, P. (2018). Deep learning to represent subgrid processes in climate models. *Proceedings of the National Academy of Sciences*, *115*(39), 9684–9689. https://doi.org/10.1073/pnas.1810286115
- Ruppert, J. H. (2016). Diurnal timescale feedbacks in the tropical cumulus regime. *Journal of Advances in Modeling Earth Systems*, 8(3), 1483–1500. https://doi.org/10.1002/2016MS000713
- Ravuri, S., Lenc, K., Willson, M., Kangin, D., Lam, R., Mirowski, P., et al. (2021). Skilful precipitation nowcasting using deep generative models of radar. *Nature*, *597*(7878), 672–677. https://doi.org/10.1038/s41586-021-03854-z
- Schultz, M. G., Betancourt, C., Gong, B., Kleinert, F., Langguth, M., Leufen, L. H., et al. (2021). Can deep learning beat numerical weather prediction? *Philosophical Transactions of the Royal Society A: Mathematical, Physical and Engineering Sciences*, *379*(2194), 20200097. https://doi.org/10.1098/rsta.2020.0097
- Shi, X., Chen, Z. W., Yeung, D.-Y., Wong, W., & WOO, W. (2015). Convolutional LSTM network: A machine learning approach for precipitation nowcasting. *Advances in Neural Information Processing Systems*, 28, 802–810.
- Shiu, C.-J., Wang, Y.-C., Hsu, H.-H., Chen, W.-T., Pan, H.-L., Sun, R., et al. (2021). GTS v1.0: A macrophysics scheme for climate models based on a probability density function. *Geoscientific Model Development*, *14*(1), 177–204. https://doi.org/10.5194/gmd-14-177-2021

- Skamarock, W. C., Klemp, J. B., Duda, M. G., Fowler, L. D., Park, S.-H., & Ringler, T. D. (2012). A multiscale nonhydrostatic atmospheric model using centroidal voronoi tesselations and C-grid staggering. *Monthly Weather Review*, *140*(9), 3090–3105. https://doi.org/10.1175/MWR-D-11-00215.1
- Slingo, J., Inness, P., Neale, R., Woolnough, S., & Yang, G. (2003). Scale interactions on diurnal to seasonal timescales and their relevance to model systematic errors. *Annals of Geophysics*, 46(1). https://doi.org/10.4401/ag-3383
- Song, Y., Chen, G., & Wang, W.-C. (2019). Aerosol direct radiative and cloud adjustment effects on surface climate over eastern China: Analyses of WRF model simulations. *Journal of Climate*, 32(4), 1293–1306. https://doi.org/10.1175/jcli-d-18-0236.1
- Stephens, G. L., Vane, D. G., Boain, R. J., Mace, G. G., Sassen, K., Wang, Z., et al. (2002). The CloudSat mission and the A-Train: A new dimension of space-based observations of clouds and precipitation. Bulletin of the American Meteorological Society, 83(12), 1771–1790. https://doi.org/10.1175/BAMS-83-12-1771
- Stevens, B., & Feingold, G. (2009). Untangling aerosol effects on clouds and precipitation in a buffered system. *Nature*, 461(7264), 607–613. https://doi.org/10.1038/nature08281
- Stevens, B., Sherwood, S. C., Bony, S., & Webb, M. J. (2016). Prospects for narrowing bounds on Earth's equilibrium climate sensitivity. *Earth's Future*, *4*(11), 512–522. https://doi.org/10.1002/2016EF000376
- Schuddeboom, A. J., & McDonald, A. J. (2021). The Southern Ocean radiative bias, cloud compensating errors, and equilibrium climate sensitivity in CMIP6 models. *Journal of Geophysical Research: Atmospheres*, 126(22). https://doi.org/10.1029/2021JD035310
- Sundqvist, H., Berge, E., & Kristjánsson, J. E. (1989). Condensation and cloud parameterization studies with a mesoscale numerical weather prediction model. *Monthly Weather Review*, 117(8), 1641–1657. <a href="https://doi.org/10.1175/1520-0493(1989)117<1641:cacpsw>2.0.co;2">https://doi.org/10.1175/1520-0493(1989)117<1641:cacpsw>2.0.co;2
- Tang, Y., Zhou, Y., Cai, M., Ma, Q. (2020). Global distribution of clouds based on CloudSat and CALIPSO combined observations. *Trans Atmos Sci*, 43(5), 917-931. https://doi.org/10.13878/j.cnki.dqkxxb.20180104001. (In Chinese).
- Tiedtke, M. (1993). Representation of clouds in large-scale models. *Monthly Weather Review*, *121*(11), 3040–3061. <a href="https://doi.org/10.1175/1520-0493(1993)121<3040:rocils>2.0.co;2">https://doi.org/10.1175/1520-0493(1993)121<3040:rocils>2.0.co;2
- Vignesh, P. P., Jiang, J. H., Kishore, P., Su, H., Smay, T., Brighton, N., & Velicogna, I. (2020). Assessment of CMIP6 cloud fraction and comparison with satellite observations. *Earth and Space Science*, 7(2). https://doi.org/10.1029/2019EA000975
- Wang, J., Balaprakash, P., & Kotamarthi, R. (2019). Fast domain-aware neural network emulation of a planetary boundary layer parameterization in a numerical weather forecast model. *Geosci. Model Dev.*, 12(10), 4261–4274. https://doi.org/10.5194/gmd-12-4261-2019
- Wang, M., & Zhang, G. J. (2018). Improving the simulation of tropical convective cloud-top heights in CAM5 with CloudSat observations. *Journal of Climate*, *31*, 5189–5204. https://doi.org/10.1175/JCLI-D-18-0027.1

- Wang, X., Miao, H., Liu, Y., & Bao, Q. (2021). Dependence of cloud radiation on cloud overlap, horizontal inhomogeneity, and vertical alignment in stratiform and convective regions. *Atmospheric Research*, 249, 105358. https://doi.org/10.1016/j.atmosres.2020.105358
- Wang, Y., Yang, S., Chen, G., Bao, Q., & Li, J. (2023). Evaluating two diagnostic schemes of cloud-fraction parameterization using the CloudSat data. *Atmospheric Research*, 282, 106510. https://doi.org/10.1016/j.atmosres.2022.106510
- Weisz, E., Li, J., Menzel, W. P., Heidinger, A. K., Kahn, B. H., & Liu, C.-Y. (2007). Comparison of AIRS, MODIS, CloudSat and CALIPSO cloud top height retrievals. *Geophysical Research Letters*, 34(17), L17811. https://doi.org/10.1029/2007GL030676
- Wild, M., Hakuba, M. Z., Folini, D., Dörig-Ott, P., Schär, C., Kato, S., & Long, C. N. (2019). The cloud-free global energy balance and inferred cloud radiative effects: An assessment based on direct observations and climate models. *Climate Dynamics*, *52*, pages4787-4812. https://doi.org/10.1007/s00382-018-4413-y
- Wilson, D. R., Bushell, A. C., Kerr-Munslow, A. M., Price, J. D., & Morcrette, C. J. (2008). PC2: A prognostic cloud fraction and condensation scheme. I: Scheme description. *Quarterly Journal of the Royal Meteorological Society*, *134*(637), 2093–2107. https://doi.org/10.1002/qj.333
- Xu, K.-M., & Randall, D. A. (1996). A semiempirical cloudiness parameterization for use in climate models. *Journal of the Atmospheric Sciences*, *53*(21), 3084–3102. https://doi.org/10.1175/1520-0469(1996)053<3084:ascpfu>2.0.co;2
- Xue, H. W., Feingold, G., & Stevens, B. (2008). Aerosol effects on clouds, precipitation, and the organization of shallow cumulus convection. *Journal of the Atmospheric Sciences*, 65(2), 392–406. https://doi.org/10.1175/2007jas2428.1
- Yang, J., Wang, W.-C., Chen, G., Bao, Q., Qi, X., & Zhou, S. (2018). Intraseasonal variation of the black carbon aerosol concentration and its impact on atmospheric circulation over the southeastern Tibetan Plateau. *Journal of Geophysical Research: Atmospheres*, 123(19). https://doi.org/10.1029/2018JD029013
- Yin, Y., Carslaw, K. S., & Feingold, G. (2005). Vertical transport and processing of aerosols in a mixed-phase convective cloud and the feedback on cloud development. *Quarterly Journal of the Royal Meteorological Society*, *131*(605), 221–245. https://doi.org/10.1256/qj.03.186
- Zhang, F., Liang, X.-Z., Li, J., & Zeng, Q. (2013). Dominant roles of subgrid-scale cloud structures in model diversity of cloud radiative effects. *Journal of Geophysical Research: Atmospheres*, *118*(14), 7733–7749. https://doi.org/10.1002/jgrd.50604
- Zhang, H., & Jing, X. (2016). Advances in studies of cloud overlap and its radiative issues in the climate models. *Acta Meteorologica Sinica*, 74(1), 103–113. (In Chinese) https://doi.org/10.11676/qxxb2016.009
- Zhang, J., Liu, P., Zhang, F., & Song, Q. (2018). Cloudnet: Ground-based cloud classification with deep convolutional neural network. *Geophysical Research Letters*, 45(16), 8665–8672. https://doi.org/10.1029/2018GL077787
- Zhang, T., Lin, W., Vogelmann, A. M., Zhang, M., Xie, S., Qin, Y., & Golaz, J. (2021). Improving convection trigger functions in deep convective parameterization schemes using

- machine learning. *Journal of Advances in Modeling Earth Systems*, *13*(5). https://doi.org/10.1029/2020MS002365
- Zhang, Y., Wu, K., Zhang, J., Zhang, F., Xiao, H., Wang, F., et al. (2021). Estimating rainfall with multi-resource data over East Asia based on machine learning. *Remote Sensing*, 13(16), 3332. https://doi.org/10.3390/rs13163332
- Zhou, L., Bao, Q., Liu, Y., Wu, G., Wang, W.-C., Wang, X., et al. (2015). Global energy and water balance: Characteristics from Finite-volume Atmospheric Model of the IAP/LASG (FAMIL1). *Journal of Advances in Modeling Earth Systems*, 7(1), 1–20. https://doi.org/10.1002/2014ms000349
- Zhou, Y., Zhang, Y., Li, J., Yu, R., & Liu, Z. (2020). Configuration and evaluation of a global unstructured mesh atmospheric model (GRIST-A20.9) based on the variable-resolution approach. *Geoscientific Model Development*, *13*(12), 6325–6348. https://doi.org/10.5194/gmd-13-6325-2020